JACS
JOURNAL OF THE AMERICAN CHEMICAL SOCIETY

Article

pubs.acs.org/JACS

In-Situ Probe of Gate Dielectric-Semiconductor Interfacial Order in Organic Transistors: Origin and Control of Large Performance Sensitivities

Stephanie R. Walter,[†,∥] Jangdae Youn,[†,∥] Jonathan D. Emery,[‡] Sumit Kewalramani,[‡] Jonathan W. Hennek,[†] Michael J. Bedzyk,*[,‡,§] Antonio Facchetti,*[,†] Tobin J. Marks,*[,†] and Franz M. Geiger*[,†]

[†]Department of Chemistry and the Materials Research Center, Northwestern University, 2145 Sheridan Rd., Evanston, Illinois 60208-3113, United States

[‡]Department of Materials Science and Engineering, Northwestern University, Evanston, Illinois 60208, United States

[§]Department of Physics and Astronomy, Northwestern University, Evanston, Illinois, 60208, United States

Supporting Information

ABSTRACT: Organic thin film transistor (OTFT) performance is highly materials interface-dependent, and dramatic performance enhancements can be achieved by properly modifying the semiconductor/gate dielectric interface. However, the origin of these effects is not well understood, as this is a classic "buried interface" problem that has traditionally been difficult to address. Here we address the question of how *n*-octadecylsilane (OTS)–derived self-assembled monolayers (SAMs) on Si/SiO_2 gate dielectrics affect the OTFT performance of the archetypical small-molecule p-type semiconductors P-BTDT (phenylbenzo[*d*,*d*]thieno[3,2-*b*;4,5-*b*]dithiophene) and pentacene using combined in situ sum frequency generation spectroscopy, atomic force microscopy, and grazing incidence and reflectance X-ray scattering. The molecular order and orientation of the OTFT components at the dielectric/semiconductor interface is probed as a function of SAM growth mode in order to understand how this impacts the overlying semiconductor growth mode, packing, crystallinity, and carrier mobility, and hence, transistor performance. This understanding, using a new, humidity-specific growth procedure, leads to a reproducible, scalable process for highly ordered OTS SAMs, which in turn nucleates highly ordered p-type semiconductor film growth, and optimizes OTFT performance. Surprisingly, the combined data reveal that while SAM molecular order dramatically impacts semiconductor crystalline domain size and carrier mobility, *it does not significantly influence the local orientation of the overlying organic semiconductor molecules.*

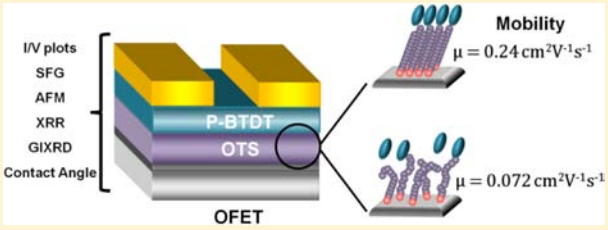

INTRODUCTION

Organic thin film transistors (OTFTs) offer many attractions for unconventional electronic circuitry,[1] including solution-processability/printability,[2] mechanical flexibility,[3] fabrication at low temperatures,[4] low production costs via roll-to-roll printing,[5] biocompatibility,[6] and high performance.[7] In these devices, charge carriers are created in a thin semiconductor channel at the interface with the gate dielectric via a field-effect mechanism,[1e,h,6c,7e] with a representative bottom-gate/top-contact OTFT architecture shown in Figure 1a. While the dielectric/semiconductor interfacial structure is of great significance for OTFT performance because it strongly affects charge transport within the proximate semiconducting channel,[7a,8] such buried interfaces are poorly understood at the molecular level and, indeed, unambiguous in situ structural characterization of such functional interfaces presents a daunting challenge.[1f,9] As recently demonstrated by Massari and co-workers,[10] the nonlinear optical probe, vibrational sum frequency generation (SFG) spectroscopy, offers a powerful tool for advancing the molecular level understanding of important interfaces in electronically functional organic materials. Here we present the results of an interface-specific characterization study, combining SFG, atomic force microscopy (AFM), grazing-incidence X-ray diffraction (GIXRD), X-ray reflectivity (XRR), and OTFT electrical measurements,

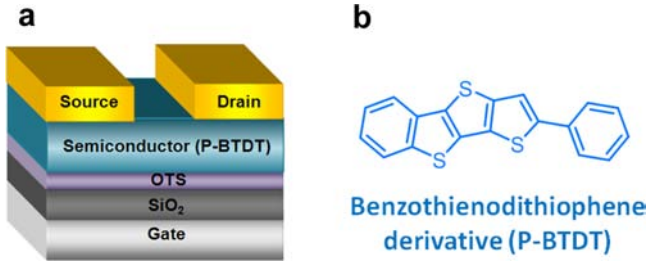

Figure 1. Components of organic thin film transistors fabricated with n-octadecylsilane (OTS)-functionalized gate dielectrics. a. Sketch of a bottom-gate/top-contact OTFT device architecture. b. Molecular structure of the organic semiconductor P-BTDT.

Received: April 25, 2012
Published: June 18, 2012

   dx.doi.org/10.1021/ja3036493 | J. Am. Chem. Soc. 2012, 134, 11726–11733

aimed at understanding how gate dielectric microstructure and growth affect OTFT performance for an archetypical small-molecule semiconductor. Importantly, we show that while molecular order within self-assembled monolayer (SAM) coatings on Si/SiO_2 gate dielectrics dramatically impacts the semiconductor interfacial growth morphology, hence TFT performance, *it does not affect the semiconductor molecular orientation*. To achieve optimum control over SAM growth, we also report a new, efficient, and scalable humidity controlled method of growing highly ordered OTS SAMs, and show that it provides optimal OTFT performance.

A major advance in OTFT dielectric/semiconductor interfacial modification has been the chemisorption of alkylsilane SAMs onto SiO_2 gate dielectric surfaces, reducing both the density of charge trapping sites and the SiO_2 surface energy, thereby increasing microstructural order in the overlying semiconductor films.[11] Thus, *n*-octadecylsilane (OTS)-based SAMs significantly enhance OTFT performance,[12] with the degree of enhancement reflecting changes in the SAM microstructural order.[13] Previous studies aimed at understanding these effects relied heavily on GIXRD to characterize variations in OTS SAM order. While GIXRD is a powerful nanoscale characterization tool, it is inherently limited since it only samples the crystalline, that is, the intrinsically ordered portions of the SAM.[11b] Vibrational techniques such as attenuated total reflectance-IR spectroscopy have also been employed to characterize SAM geometries (e.g., the *gauche* defect number density in *n*-alkyl structures[14]), however they are not based on vibrational coherences and therefore have limited access to molecular orientations, especially in buried interfaces.[11b,13b,14] Here, the crystalline as well as noncrystalline portions of the OTS layer in the buried interface are probed by a combination of AFM, GIXRD, XRR, and SFG. While XRR specifically quantifies the electron density profile along the substrate normal, and therefore indirectly reveals the average molecular orientation, SFG *directly probes local intramolecular conformation*.

Vibrational SFG is a coherent, surface-specific spectroscopy that is exquisitely sensitive to interfacial molecular order and orientation.[15] Since SFG is a second-order nonlinear spectroscopy, the selection rules dictate that signals only arise from noncentrosymmetric motifs, such as at interfaces, making it a powerful tool for assessing order within alkyl monolayers,[16] and for tracking organic semiconductor film microstructural changes.[17] A key insight from *n*-alkyl SAM studies is that the CH_2 stretching modes are SFG-inactive in well-ordered, all-*trans*-configured alkyl chains due to the local inversion centers in the C−C bonds.[16c] Thus, the SFG spectra of well-ordered, all-*trans* *n*-alkyl monolayers, as prepared by the present growth technique, exhibit strong features for CH_3 stretching modes, and little or no contribution from CH_2 stretching modes. In contrast, disordered monolayers contain *gauche* defects along the carbon backbone that disrupt the local inversion centers, and the CH_2 stretching modes become SFG active.[16b,c] Here we apply these capabilities for the first time, combined with AFM, GIXRD, and XRR, to resolve the issue of how SAM order affects performance in small-molecule OTFTs fabricated with OTS-coated SiO_2 gate dielectrics.

EXPERIMENTAL SECTION

Materials. Octadecyltrichlorosilane (OTS) was purchased from Sigma-Aldrich. Co. (90%) and used as received. Device substrates consisted of heavily doped Si wafers with 300 nm of thermally grown silicon oxide having a capacitance per unit area (C_i) of 10 $nFcm^{-2}$. P-BTDT was generously provided by Prof M.-C. Chen of National Central University, Taiwan.[18]

OTS SAM Fabrication. A 300 nm Si/SiO_2 substrate was used after ethanol washing and O_2 plasma cleaning. Solution process methods were used as an alternative to vapor phase silanization, which has been shown to induce low surface coverages and disorganized SAM structures.[13b] For anhydrous (AA-OTS) SAM fabrication, the Si/SiO_2 substrates were immersed in 3.0 mM dry toluene solutions of the silane reagent under N_2 for 10 h after the O_2 plasma. Then the substrates were sonicated with toluene, acetone, and ethanol, followed by drying in a N_2 stream. Notably, while anhydrous conditions are expected to produce smooth OTS SAMs with minimal aggregation, SAM formation is sluggish. Therefore, to best obtain full surface coverage of AA-OTS, these substrates were left in OTS solutions for longer deposition times than for humidity-controlled SAMs (10 h vs 1 h). To fabricate humidity-specific OTS-coated substrates, including high humidity (HH-OTS) SAMs, growth was performed under ambient conditions in a controlled atmosphere glovebox at varied relative humidity levels ranging from 4 to 85%. First, a 3.0 mM OTS-hexane solution was left standing in air for 10 h under the relative humidity conditions shown in Figure 2, with

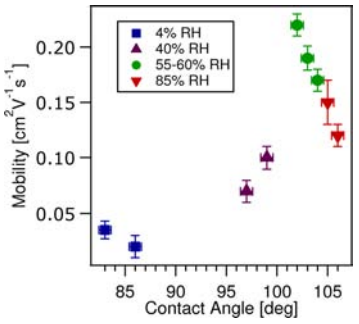

Figure 2. OTFT field-effect mobility as a function of OTS growth conditions, expressed by relative humidity (% RH) during growth. Bars indicate experimental uncertainties.

55−60% relative humidity used for the HH-OTS films. The Si/SiO_2 substrates were then introduced into the humidity-controlled chamber and immediately immersed in the OTS-hexane solution for 1 h. The effect of water adsorption on the Si/SiO_2 substrate due to standing in the humidity chamber before immersion in the OTS solution was found to be negligible based on TFT performance. Following OTS deposition, substrates were then sonicated with hexane, acetone, and ethanol, followed by drying in an N_2 stream. Monolayer formation was confirmed with XRR, GIXRD, and SFG.

SAM Characterization. To image film surface morphologies, AFM measurements were performed by using a Dimension Icon Scanning Probe Microscope (Veeco) in the tapping mode (Supporting Information (SI) Figures S1−S3). Contact angle measurements were performed on a First Ten Angstroms (FTA 125) goniometer. GIXRD and XRR experiments were carried out on an 18 kW Rigaku ATXG diffractometer using a multilayer parabolic mirror, an NaI scintillation detector, and X-rays of wavelength λ = 1.541 Å. Coherent vibrational spectroscopy was performed with an 800 nm, 120 fs regeneratively amplified Ti:Sapphire system (Spitfire

dx.doi.org/10.1021/ja3036493 | J. Am. Chem. Soc. 2012, 134, 11726−11733

Table 1. P-BTDT TFT Performance Data As a Function of Gate Dielectric Surface Treatment[a]

	vacuum			air		
dielectric surface treatment	mobility ($cm^2V^{-1}s^{-1}$)	threshold voltage (V)	I_{on}/I_{off}	mobility ($cm^2V^{-1}s^{-1}$)	threshold voltage (V)	I_{on}/I_{off}
bare SiO_2	0.078(3) max = 0.081	−30(6)	$3(1) \times 10^6$	0.074(9) max = 0.085	−22(2)	$10(4) \times 10^6$
AA-OTS	0.072(9) max = 0.080	−33(3)	$6(4) \times 10^7$	0.085(4) max = 0.090	−41(5)	$1.6(4) \times 10^8$
HH-OTS	0.24(6) max = 0.310	−36(7)	$3(2) \times 10^8$	0.22(3) max = 0.250	−41(8)	$4(3) \times 10^8$

[a]Parentheses indicate experimental uncertainties.

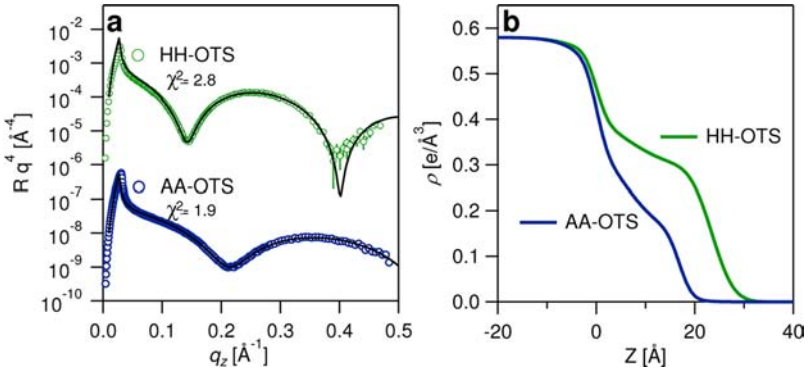

Figure 3. a. XRR data and corresponding fits for HH-OTS (green) and AA-OTS (blue) SAM-coated substrates. The data for HH-OTS have been shifted vertically (×10^4) for clarity. The fits were performed over a q_z range of 0.1−0.47 $Å^{-1}$ using a two-slab model under the kinematic Born approximation. b. The best-fit e-density profiles for the HH- OTS (green) and LH-OTS (blue) SAMs. Note that the features pertaining to the silane headgroup layer are smeared because the roughnesses at the substrate-silane and silane-alkyl tail interface are comparable to the thickness of this layer (SI Table S2).

Pro, Spectra Physics, 2.5 mJ/pulse) with a 1 kHz repetition rate, which was used to pump an optical parametric amplifier (OPA-800CF, Spectra Physics) producing broadband IR laser light around 3.4 μm with a bandwidth (full width at half-maximum) of ∼140 cm^{-1}. Further experimental details and data can be found in the SI.

OTFT Fabrication. Thin film transistors were fabricated in the bottom-gate/top-contact configuration. Highly doped p-type (100) silicon wafers (<0.004 Ωcm) were used as gate electrodes as well as substrates, and 300 nm SiO_2 thermally grown on Si was used as the gate insulator. The unit area capacitance is 10 $nFcm^{-2}$. OTS SAMs were deposited, as described above, prior to semiconductor deposition. Semiconductor thin films (50 nm) were next vapor-deposited onto the substrates held at a predetermined temperature of 25 °C for P-BTDT with a deposition rate of 0.1 Å/s at 6×10^{-6} Torr, employing a high-vacuum deposition chamber (Denton Vacuum, Inc., Moorestown, NJ). Gold source and drain electrodes (50 nm) were vapor-deposited at 2×10^{-6} Torr through a shadow mask in the vacuum deposition chamber. Devices were fabricated with typical channel lengths of 100 μm, and a channel width of 5000 μm.

OTFT Characterization. $I-V$ plots of device performance were measured in air and in vacuum, and transfer and output plots were recorded for each device. The current−voltage ($I-V$) characteristics of the devices were measured using a Keithley 6430 subfemtoammeter and a Keithly 2400 source meter, driven by a local Labview program and GPIB communication. Key device parameters, such as charge carrier mobility (μ) and on-to-off current ratio (I_{on}/I_{off}), were extracted from the source-drain current (I_{SD}) versus source-gate voltage (V_{SG}) characteristics employing standard procedures.[19] Mobilities were obtained from the formula $\mu = 2I_{SD}L/[C_iW(V_{SG}-V_T)^2]$, defined by the saturation regime in transfer plots, where I_{SD} is the source-drain current, V_{SG} is source-gate voltage, and V_T is the threshold voltage. Threshold voltage was obtained from the x intercept of V_{SG} vs $I_{SD}^{1/2}$ plots. SI Figure S4 illustrates a representative $I-V$ curve for devices fabricated with HH-OTS.

RESULTS AND DISCUSSION

For this study, *n*-octadecyltrichlorosilane-derived monolayers are grown on 300 nm Si/SiO_2 substrates under humidity specific conditions, as detailed in the Experimental Section. Briefly, OTS SAMs grown in an anhydrous atmosphere, denoted AA-OTS, are produced by depositing OTS in dry conditions under an N_2 atmosphere. All other samples were prepared in a humidity-controlled glovebox under relative humidity (RH) conditions ranging from 4 to 85%. The highest performing OTFTs were fabricated with OTS SAMs deposited at 55−60% relative humidity and are designated as high-humidity OTS (HH-OTS) SAMs. OTS SAM microstructure was characterized by aqueous contact angle goniometry, GIXRD, XRR, tapping mode AFM, and SFG spectroscopy (see SI for details). Subsequently, semiconductor thin films of phenylbenzo[*d*,*d*]thieno[3,2-*b*;4,5-*b*]dithiophene (P-BTDT; Figure 1b)[18] were vacuum-deposited onto the OTS-functionalized substrates. P-BTDT was chosen here because fused thiophene-based materials present high-mobility, environmentally stable alternatives to pentacene,[18] and because the asymmetric molecular structure makes it an ideal interfacial SFG probe. Pentacene devices were also fabricated to probe the generality of the SAM HH-OTS growth procedure on OTFT performance. Gold source and drain electrodes were vapor-deposited to fabricate TFTs in the bottom-gate/top-contact configuration (Figure 1a).

To specifically examine correlations between OTFT performance, humidity during SAM growth, and OTS surface chemical properties, OTS SAMs were grown under different levels of ambient relative humidity (4−85%) to examine the effects that variations in the monolayer structure have on

dx.doi.org/10.1021/ja3036493 | J. Am. Chem. Soc. 2012, 134, 11726−11733

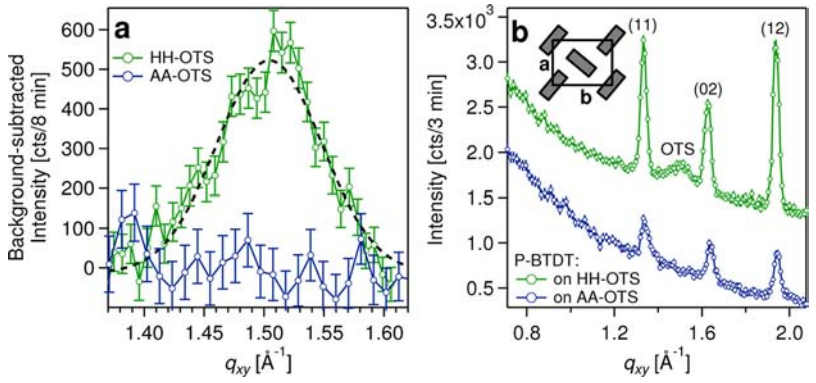

Figure 4. GIXRD characterization of the in-plane packing of molecules in the OTS SAMs and the P-BTDT semiconducting layer. a. Background-subtracted GIXRD data from AA-OTS (blue) and HH-OTS (green) SAMs. The dotted line is the Gaussian fit to the HH-OTS diffraction peak. b. GIXRD from a 3 nm P-BTDT film on HH-OTS (top, green) and AA-OTS (bottom, blue). Inset shows a schematic of the molecular projection of P-BTDT onto the 2D in-plane lattice, illustrating the herringbone molecular packing. The data shown in the above figures is integrated over q_z = 0.01−0.14 Å^{-1}. However, for P-BTDT on HH-OTS, synchrotron GIXRD data (not shown) were also collected over the range q_{xy} ∼ 0−3.0 Å^{-1} and q_z ∼ 0−2.0 Å^{-1} using a 2D area detector. No additional diffraction peaks from ordering of the OTS alkyl tails were observed. Two additional, but weak in-plane diffraction peaks from P-BTDT crystals were observed at q_{xy} ∼ 2.10 Å^{-1} and ∼2.66. Å^{-1}, which correspond to the (2 0) and (2 2) reflections.

OTFT electrical properties. Figure 2 shows that controlled humidity deposition of OTS SAMs directly correlates with subsequent contact angle measurements. Importantly, OTS SAMs grown under 55−60% RH conditions (HH-OTS) exhibit a narrow contact angle range of 102−104°, which correlates with a maximum field-effect carrier mobility of 0.22(1) $cm^2V^{-1}s^{-1}$. Such optimization is reasonable since at low RH there is insufficient water content to promote effective grafting of the silanes, while at very high RH excess water can promote the formation of aggregates. Figure 2 does not include measurements from OTFTs fabricated on AA-OTS (RH = 0%) because of the much longer deposition time required (10 h vs 1 h) to achieve OTS monolayers under completely anhydrous conditions. Note that the advancing aqueous contact angle data also show that the HH-OTS monolayers are consistently more hydrophobic than the AA-OTS counterparts (SI Figure S5), likely reflecting variations in surface structure due to differences in OTS microstructural characteristics. Furthermore, the transistor current−voltage (I−V) data reveal a significant divergence in performance between AA-OTS and HH-OTS-based OTFTs. Table 1 shows that the mobility measured under vacuum increases from 0.072(9) $cm^2V^{-1}s^{-1}$ for AA-OTS-based OTFTs to 0.24(6) $cm^2V^{-1}s^{-1}$ for HH-OTS-based devices, indicating a strong OTFT performance enhancement with the humidity-selective OTS growth. Similar results are obtained when the devices are measured in air. The results shown in Table 1 were obtained from a grand total of 40 different OTFTs, where the number in parentheses indicates the standard deviation (1σ) associated with the last digit of the value. From these results, the contact angle measurements are clearly a very useful qualitative index of optimal OTS monolayer microstructure for OTFT performance. Nevertheless, more sensitive and informative structural methods are required for a deeper understanding; thus, we employ XRR, GIXRD, and vibrational SFG.

Figure 3a shows the XRR data for the HH-OTS and the AA-OTS SAMs as a function of q_z, the scattering vector component along the substrate normal. The solid lines are the best fits obtained using the "standard" two box model for the in-plane averaged electron density profile $\rho(z)$. Physically, the two boxes in the model represent the silane headgroup and the alkyl tail layers of the OTS SAMs. Following Fukuto et al.,[20] the physically relevant parameters of the model, namely the electron densities and thicknesses of the headgroup and alkyl tail layers were extracted from the extremum positions in the best-fit electron density profiles (Figure 3b) and their derivatives. The two box fitting parameters are detailed separately in SI Table S2. The profile-derived electron densities and thicknesses for the alkyl chain layers are $0.31^{+0.02}_{-0.01}$ $e^-/Å^3$ and $22.6^{+0.9}_{-2.3}$ Å, respectively, for HH-OTS SAMs and $0.18^{+0.06}_{-0.01}$ $e^-/Å^3$ and $16.6^{+0.6}_{-3.0}$ Å, respectively, for AA-OTS SAMs. For the alkyl tail layer of HH-OTS, the derived thickness is close to the expected length of 17 × 1.27 Å = 21.6 Å for a fully *trans*-configured 18-carbon chain, and the electron density is close to that of a close-packed linear alkane (0.32 $e^-/Å^3$).[21] These observations suggest a solid-like packing of untilted alkyl tails in HH-OTS. In contrast, the electron density and thickness of the alkyl tail region of AA-OTS are much lower, suggesting a sparsely packed layer of liquid-like disordered alkyl tails. These XRR-based interpretations are corroborated by GIXRD measurements. For HH-OTS, the clear presence of a single in-plane diffraction peak at q_{xy} ∼ 1.50 Å^{-1} implies that the untilted alkyl tails are arranged on a hexagonal lattice with a unit cell parameter of $a = 4\pi/(\sqrt{3} \times q_{xy})$ = 4.83 Å (Figure 4a). In contrast, for AA-OTS, no diffraction peak arising from the ordering of alkyl tails is observed. We therefore conclude that the HH-OTS SAM consists of closely packed OTS molecules in a crystalline arrangement, while the AA-OTS SAM is disordered, with a percent crystallinity that is below the detection limits of the experiment. To directly compare AA-OTS and HH-OTS SAMs at the molecular level, SFG spectroscopy was next employed.

Figure 5 shows SFG spectra of the AA-OTS and HH-OTS monolayers on Si/SiO_2 substrates before and after P-BTDT deposition. The spectra were obtained with a polarization combination that probes vibrational modes with transition dipole components oriented predominantly perpendicular to the surface. Spectral fitting (SI Figure S6) shows that the AA-OTS spectrum exhibits a CH_3 Fermi resonance at 2930 cm^{-1}, a CH_2 asymmetric stretching mode at 2907 cm^{-1}, a CH_3 symmetric stretching mode at 2873 cm^{-1}, and a CH_2 symmetric stretching mode at 2853 cm^{-1} (Figure 5a). In contrast, the HH-OTS spectrum exhibits a CH_3 Fermi resonance at 2940 cm^{-1} and a CH_3 symmetric stretching mode at 2880 cm^{-1}, while the

dx.doi.org/10.1021/ja3036493 | J. Am. Chem. Soc. 2012, 134, 11726−11733

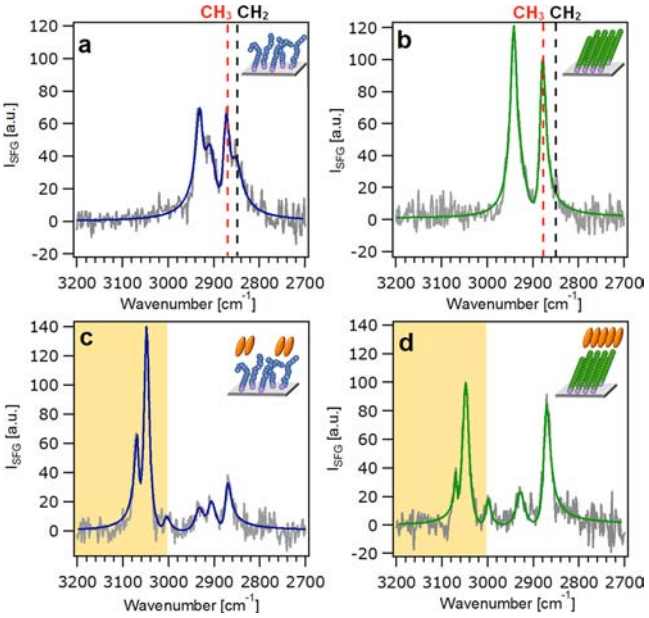

Figure 5. Typical SFG spectra of OTS SAM-functionalized gate dielectrics with and without an overlying P-BTDT organic semiconductor layer. SSP-polarized SFG spectra of a. an AA-OTS monolayer; b. an HH-OTS monolayer; c. an AA-OTS/50 nm P-BTDT bilayer; d. an HH-OTS/50 nm P-BTDT bilayer. Raw spectra are shown in gray, and fitted data shown in blue and green for surfaces covered with AA-OTS and HH-OTS, respectively. Red and black dotted lines in a and b identify CH_3 and CH_2 symmetric stretch frequencies. The shaded region above 3000 cm^{-1} indicates aromatic contributions from P-BTDT. The HH-OTS sample has a higher ratio of CH_3/CH_2 symmetric stretches, indicative of a more highly ordered system. Insets: cartoons of OTS order and P-BTDT packing for each system represented.

CH_2 asymmetric stretching mode appears as only a small shoulder at 2922 cm^{-1}, and the CH_2 symmetric stretching mode intensity is negligible (Figure 5b). These results are consistent with literature data for similar linear hydrocarbon systems and indicate that OTS SAM growth under high-humidity conditions yields films that are significantly more ordered than those grown under anhydrous conditions. The HH-OTS and AA-OTS monolayers produce strong SFG signals from the CH_3 symmetric stretching modes but not from the CH_3 asymmetric stretching mode (~2960 cm^{-1}). However, when vibrational modes with transition dipole components oriented mainly parallel to the surface are probed, the CH_3 asymmetric stretching mode yields a strong SFG signal (SI Figures S7–8), indicating that the methyl groups are oriented principally along the surface normal.

Since the SFG results show that the AA-OTS SAMs have a significant density of *gauche* defects while HH-OTS SAMs are well-ordered, we suspected that the deposition of the semiconductor might be impacted by SAM ordering, potentially compromising the P-BTDT ordering and carrier mobility on the AA-OTS substrates. Likewise, the semiconductor deposition process might also, in principle, alter the SAM ordering. We therefore investigated the impact of depositing 50 nm of P-BTDT onto the HH-OTS and AA-OTS monolayers, followed by recording the SFG spectra. These samples exhibit strong SFG signals above 3000 cm^{-1}, attributable to the P-BTDT aromatic CH stretches (Figures 5c and d). The vibrational resonances of the underlying OTS layers are still clearly discernible at frequencies below 3000 cm^{-1}, even with increasing P-BTDT film thicknesses (SI Figure S9) where it is apparent that the P-BTDT molecules adopt an anisotropic arrangement contributing to SFG signals from the bulk. Most importantly, the HH-OTS SAM remains highly ordered after the overlying P-BTDT layer growth, although there is a slight red shift in the peak frequency of the CH_3 Fermi resonance and CH_3 symmetric stretch which is likely due to the change in chemical environment as P-BTDT interacts with the more ordered/uniform methyl groups of this SAM.[22] The retention of HH-OTS ordering is in excellent agreement with the aforementioned GIXRD data on HH-OTS SAMs coated with a 3 nm P-BTDT layer, which reveal a persistent and unchanged OTS layer diffraction peak at ~1.50 $Å^{-1}$ (Figure 4b). Furthermore, the SFG results indicate that the orientation of the semiconductor at the interface is invariant with the order in the underlying SAM interfacial layer. The SSP and SPS spectra for P-BTDT on AA-OTS and HH-OTS are overlaid in SI Figure S10 to illustrate that the peak shapes and relative intensities assignable to P-BTDT (above 3000 cm^{-1}) are similar within experimental error for both SAMs. Note that for much larger changes in SAM ordering and surface properties, there is evidence of semiconductor orientational changes,[23] although this does not appear to play a major role for the present materials.

The SFG-derived conclusions on the P-BTDT molecular alignment are also supported by GIXRD measurements, which show three in-plane diffraction peaks at q_{xy} ~1.33, 1.63, and 1.94 $Å^{-1}$ (Figure 4b), for P-BTDT on HH-OTS as well as on AA-OTS. This indicates that for both SAMs, the P-BTDT molecules are arranged in a crystalline lattice, with identical lattice parameters and molecular packing arrangement. Furthermore, the packing of P-BTDT molecules in these thin films has striking similarities to the P-BTDT arrangements in the crystal structure of bulk 3D crystals.[18] First, the observed diffraction peaks can be indexed by assuming a rectangular cell with lattice constants a = 5.96 Å and b = 7.71 Å, indicating an only slightly expanded lattice versus the (001) crystallographic plane (a_b = 5.85 Å and b_b = 7.59 Å, γ = 90.2°) of P-BTDT single crystals.[18] Second, the absence of (10) and (01) reflections and the simultaneous observation of the (12) peak in the GIXRD data (Figure 4b) are indicative of a herringbone packing of molecules in a rectangular unit cell with p2gg plane group symmetry (inset, Figure 4b).[24] This is similar to the case for the P-BTDT 3D crystal, where the molecular projections onto the (001) plane clearly exhibit a herringbone motif. The aforementioned correspondence between the P-BTDT packing in thin film and 3D crystals strongly suggests that in thin films, the P-BTDT long molecular axis lies either along or very close to the substrate normal, because in P-BTDT 3D crystals, the long molecular axis is nearly parallel to the (001) direction.

While the molecular packing and orientation for P-BTDT on HH-OTS and AA-OTS SAMs are identical, there are significant differences in the crystalline quality of the thin films in the two cases, as indicated by substantial differences in the integrated intensities and line widths (σ) of the diffraction peaks (SI Table S1). In particular, the application of Scherrer's formula reveals that the average of the correlation lengths[25] along the three observed crystallographic directions (see SI Table S1), have domains of 43 ± 2 nm for P-BTDT on HH-OTS and 33 ± 3 nm for P-BTDT on AA-OTS. In addition, the differences in the integrated intensities I between the two samples can be utilized to qualitatively compare the surface coverage by crystalline

dx.doi.org/10.1021/ja3036493 | J. Am. Chem. Soc. 2012, 134, 11726–11733

domains in each because $I \propto M \times N^2 \times \sigma$, where M is the number of crystals satisfying the Bragg condition and N is the number of unit cells in each crystal.[25] For the present study, the P-BTDT films can be assumed to be nearly 2D crystalline because the average film thickness of ∼3 nm is comparable to the length of the c-axis (3.1 nm) for the P-BTDT 3D crystals.[18] Since for 2D crystals, σ scales as $(N)^{-1/2}$, the ratio of the surface coverage by crystalline domains for P-BTDT on HH-OTS and AA-OTS is $S_{HH}/S_{AA} = M_{HH} \times N_{HH}/M_{AA} \times N_{AA} = (I_{HH} \times \sigma_{HH})/(I_{AA} \times \sigma_{AA})$. From the intensities and line widths for the three diffraction peaks (SI Table S1), the average of the ratio S_{HH}/S_{AA} is found to be ∼2.6.[26]

The above analysis indicates 30% larger crystallite domain sizes for P-BTDT on HH-OTS than on AA-OTS. This finding is important because the carrier mobility in organic semiconductors has been shown to scale linearly with domain size.[27] Furthermore, the mobility is expected to increase if the interdomain regions are more ordered, that is, if the overall film crystallinity increases.[28] In this study, the GIXRD data reveal a 2.6× increase in crystallinity for P-BTDT on HH-OTS which correlates very well with a nearly 3.3× increase in the film mobility (Table 1). We therefore conclude that the semiconductor crystallinity in the OTFTs studied here is strongly driven by the molecular order within the underlying OTS monolayer. It is interesting, however, that the local molecular orientation of the semiconductor molecules within the crystalline domains does not depend on the molecular order of the OTS underlayer. A cartoon representation of this scenario is illustrated in the insets of Figures 5 and 6, where the average orientation of the organic semiconductor molecules remains the same, but the crystalline domain size is larger for HH-OTS.

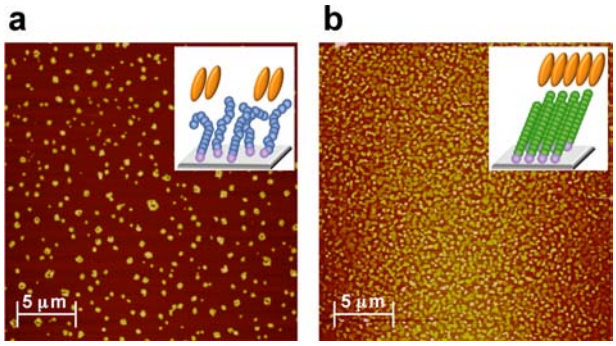

Figure 6. Surface morphologies of the initial P-BTDT growth stages. AFM images (25 × 25 μm) of 1.5 nm nominal thickness P-BTDT films grown on a. an AA-OTS monolayer; b. an HH-OTS monolayer. Insets: cartoon depiction of surface ordering for each respective system.

Complementary tapping mode AFM images illustrate the close relationship between semiconductor film surface morphology and OTFT electrical performance, as influenced by the underlying OTS layer. Given that OTFT charge transport occurs primarily within the first few monolayers of the semiconductor film proximate to the gate dielectric layer,[7a,29] AFM images were recorded during the initial P-BTDT film growth stages, as defined by a quartz crystal microbalance (Figure 6). These images clearly show that AA-OTS monolayers (Figure 6a) afford low P-BTDT nucleation densities and poor 2D growth in the initial 1.5 nm of semiconductor film versus growth on HH-OTS (Figure 6b and SI Figure S9). We attribute this promotion of high nucleation densities and extended 2D growth to the highly aligned and ordered HH-OTS monolayers, identified by the aforementioned SFG and X-ray scattering measurements, which facilitate the growth of densely packed semiconductor films and affords significantly enhanced OTFT device performance. Although AFM images of P-BTDT/AA-OTS show larger morphological grain sizes than on HH-OTS, note that morphological grain size is not always identical to crystalline domain size. Accordingly, the GIXRD data show that the crystalline domain sizes for P-BTDT on HH-OTS are significantly greater than on AA-OTS. Thus, the densely packed, largely crystalline domains of P-BTDT on HH-OTS correlate well with the enhanced mobility.

Note that we also observe the same high nucleation densities in pentacene monolayers grown on HH-OTS SAMs (SI Figure S11), which exhibit a substantial hole mobility of 1.3 $cm^2V^{-1}s^{-1}$ for 50 nm pentacene films, significantly greater than the measured μ = 0.15 $cm^2V^{-1}s^{-1}$ for pentacene on AA-OTS SAMs. This result suggests that the optimal conditions of OTS deposition as demonstrated here (RH 55−60%) have significant generality and that the ability to tailor OTS interfacial organization by controlling the relative humidity is clearly an advantageous step toward optimizing interfacial layers for individual semiconductors.

■ CONCLUSIONS

These results provide compelling evidence that the molecular order and orientation of OTS monolayers at the dielectric/semiconductor interface dramatically impact the molecular packing/growth mode and crystallinity of overlying organic semiconductor films, and hence OTFT performance. Notably, combined vibrational SFG, AFM, GIXRD, XRR, and I/V measurements show that molecular order in OTS SAMs covering the gate dielectrics dramatically impacts OTFT performance *but not the local molecular orientations in the overlying organic semiconductor*. Furthermore, we have shown how and why an OTS deposition process at 55−60% relative humidity, which affords OTS monolayers with an aqueous contact angle in the narrow range of 102−104°, promotes optimum semiconductor growth, and enhances OTFT performance. This growth process offers a reliable, efficient, and scalable method for fabricating highly ordered OTS SAMs. This level of understanding and control over interfaces, such as those presented here, is vital for the continued progress of organic electronics.

■ ASSOCIATED CONTENT

Ⓢ Supporting Information

OTS characterization by AFM, GIXRD, XRR, and SFG with various polarization combinations and of varying semiconductor thickness. This material is available free of charge via the Internet at http://pubs.acs.org.

■ AUTHOR INFORMATION

Corresponding Author

geigerf@chem.northwestern.edu; a-facchetti@northwestern.edu; bedzyk@northwestern.edu; t-marks@northwestern.edu

Author Contributions

‖These authors contributed equally.

Notes

The authors declare no competing financial interest.

■ ACKNOWLEDGMENTS

We thank AFOSR (FA9550-08-01-0331), the NSF-MRSEC program through the Northwestern Materials Research Center (DMR-1121162), and the NSF-NSEC program under Award Number EEC-0647560 for support of this research. The NSF-MRSEC program also supported use of the J.B. Cohen X-ray Diffraction Facility. We thank Prof. M.-C. Chen of National Central University, Taiwan, for generously providing a P-BTDT sample. S.R.W. acknowledges the Achievement Rewards for College Scientists (ARCS) foundation. F.M.G. acknowledges an Irving M. Klotz Professorship. We also acknowledge donations, equipment loans, and the technical support of Spectra Physics, a division of Newport Corporation and CVI Laser LCC.

■ REFERENCES

(1) (a) Anthony, J. E.; Facchetti, A.; Heeney, M.; Marder, S. R.; Zhan, X. W. *Adv. Mater.* **2010**, *22*, 3876. (b) Cho, S.; Seo, J. H.; Park, S. H.; Beaupre, S.; Leclerc, M.; Heeger, A. J. *Adv. Mater.* **2010**, *22*, 1253. (c) Facchetti, A. *Chem. Mater.* **2011**, *23*, 733. (d) Sirringhaus, H.; Bird, M.; Richards, T.; Zhao, N. *Adv. Mater.* **2010**, *22*, 3893. (e) Spijkman, M. J.; Myny, K.; Smits, E. C. P.; Heremans, P.; Blom, P. W. M.; de Leeuw, D. M. *Adv. Mater.* **2011**, *23*, 3231. (f) Virkar, A. A.; Mannsfeld, S.; Bao, Z. A.; Stingelin, N. *Adv. Mater.* **2010**, *22*, 3857. (g) Wen, Y. G.; Liu, Y. Q. *Adv. Mater.* **2010**, *22*, 1331. (h) Wen, Y. G.; Liu, Y. Q.; Guo, Y. L.; Yu, G.; Hu, W. P. *Chem. Rev.* **2011**, *111*, 3358.

(2) (a) Arias, A. C.; MacKenzie, J. D.; McCulloch, I.; Rivnay, J.; Salleo, A. *Chem. Rev.* **2010**, *110*, 3. (b) Liu, C. A.; Minari, T.; Lu, X. B.; Kumatani, A.; Takimiya, K.; Tsukagoshi, K. *Adv. Mater.* **2011**, *23*, 523. (c) Marks, T. J. *MRS Bull.* **2010**, *35*, 1018.

(3) (a) Gelinck, G.; Heremans, P.; Nomoto, K.; Anthopoulos, T. D. *Adv. Mater.* **2010**, *22*, 3778. (b) Street, R. A.; Wong, W. S.; Ready, S. E.; Chabinyc, I. L.; Arias, A. C.; Limb, S.; Salleo, A.; Lujan, R. *Mater. Today* **2006**, *9*, 32. (c) Zschieschang, U.; Ante, F.; Yamamoto, T.; Takimiya, K.; Kuwabara, H.; Ikeda, M.; Sekitani, T.; Someya, T.; Kern, K.; Klauk, H. *Adv. Mater.* **2010**, *22*, 982.

(4) Murphy, A. R.; Frechet, J. M. J. *Chem. Rev.* **2007**, *107*, 1066.

(5) (a) Kjellander, B. K. C.; Smaal, W. T. T.; Anthony, J. E.; Gelinck, G. H. *Adv. Mater.* **2010**, *22*, 4612. (b) Sun, J.; Zhang, B.; Katz, H. E. *Adv. Funct. Mater.* **2011**, *21*, 29.

(6) (a) Irimia-Vladu, M.; Troshin, P. A.; Reisinger, M.; Shmygleva, L.; Kanbur, Y.; Schwabegger, G.; Bodea, M.; Schwodiauer, R.; Mumyatov, A.; Fergus, J. W.; Razumov, V. F.; Sitter, H.; Sariciftci, N. S.; Bauer, S. *Adv. Funct. Mater.* **2010**, *20*, 4069. (b) Roberts, M. E.; Sokolov, A. N.; Bao, Z. N. *J. Mater. Chem.* **2009**, *19*, 3351. (c) Sokolov, A. N.; Tee, B. C. K.; Bettinger, C. J.; Tok, J. B. H.; Bao, Z. *Acc. Chem. Res.* **2012**, *45*, 361.

(7) (a) DiBenedetto, S. A.; Facchetti, A.; Ratner, M. A.; Marks, T. J. *Adv. Mater.* **2009**, *21*, 1407. (b) Giri, G.; Verploegen, E.; Mannsfeld, S. C. B.; Atahan-Evrenk, S.; Kim, D. H.; Lee, S. Y.; Becerril, H. A.; Aspuru-Guzik, A.; Toney, M. F.; Bao, Z. A. *Nature* **2011**, *480*, 504. (c) Lee, W. H.; Cho, J. H.; Cho, K. *J. Mater. Chem.* **2010**, *20*, 2549. (d) Osaka, I.; Zhang, R.; Sauve, G.; Smilgies, D. M.; Kowalewski, T.; McCullough, R. D. *J. Am. Chem. Soc.* **2009**, *131*, 2521. (e) Shao, W.; Dong, H. L.; Jiang, L.; Hu, W. P. *Chem Sci* **2011**, *2*, 590. (f) Tsao, H. N.; Cho, D.; Andreasen, J. W.; Rouhanipour, A.; Breiby, D. W.; Pisula, W.; Müllen, K. *Adv. Mater.* **2009**, *21*, 209.

(8) (a) Liao, K. C.; Ismail, A. G.; Kreplak, L.; Schwartz, J.; Hill, I. G. *Adv. Mater.* **2010**, *22*, 3081. (b) Zschieschang, U.; Ante, F.; Schlorholz, M.; Schmidt, M.; Kern, K.; Klauk, H. *Adv. Mater.* **2010**, *22*, 4489. (c) Marchl, M.; Edler, M.; Haase, A.; Fian, A.; Trimmel, G.; Griesser, T.; Stadlober, B.; Zojer, E. *Adv. Mater.* **2010**, *22*, 5361. (d) Di, C.-A.; Liu, Y.; Yu, G.; Zhu, D. *Acc. Chem. Res.* **2009**, *42*, 1573. (e) Ono, S.; Minder, N.; Chen, Z.; Facchetti, A.; Morpurgo, A. F. *Appl. Phys. Lett.* **2010**, *97*, 143307. (f) Gershenson, M. E.; Podzorov, V.; Morpurgo, A. F. *Rev. Mod. Phys.* **2006**, *78*, 973. (g) Hulea, I. N.; Fratini, S.; Xie, H.; Mulder, C. L.; Iossad, N. N.; Rastelli, G.; Ciuchi, S.; Morpurgo, A. F. *Nat. Mater.* **2006**, *5*, 982.

(9) (a) DeLongchamp, D. M.; Kline, R. J.; Fischer, D. A.; Richter, L. J.; Toney, M. F. *Adv. Mater.* **2011**, *23*, 319. (b) Manaka, T.; Lim, E.; Tamura, R.; Iwamoto, M. *Nat Photon* **2007**, *1*, 581. (c) Manaka, T.; Liu, F.; Weis, M.; Iwamoto, M. *Phys. Rev. B* **2008**, *78*, 121302. (d) Mannsfeld, S. C. B.; Tang, M. L.; Bao, Z. A. *Adv. Mater.* **2011**, *23*, 127. (e) Mathijssen, S. G. J.; Spijkman, M. J.; Andringa, A. M.; van Hal, P. A.; McCulloch, I.; Kemerink, M.; Janssen, R. A. J.; de Leeuw, D. M. *Adv. Mater.* **2010**, *22*, 5105. (f) Rivnay, J.; Jimison, L. H.; Northrup, J. E.; Toney, M. F.; Noriega, R.; Lu, S. F.; Marks, T. J.; Facchetti, A.; Salleo, A. *Nat. Mater.* **2009**, *8*, 952. (g) Salleo, A.; Kline, R. J.; DeLongchamp, D. M.; Chabinyc, M. L. *Adv. Mater.* **2010**, *22*, 3812.

(10) (a) Anglin, T. C.; O'Brien, D. B.; Massari, A. M. *J. Phys. Chem. C* **2010**, *114*, 17629. (b) Eigner, A. A.; Anglin, T. C.; Massari, A. M. *J. Phys. Chem. C* **2010**, *114*, 12308.

(11) (a) Dhagat, P.; Haverinen, H. M.; Kline, R. J.; Jung, Y.; Fischer, D. A.; DeLongchamp, D. M.; Jabbour, G. E. *Adv. Funct. Mater.* **2009**, *19*, 2365. (b) Yang, H. C.; Shin, T. J.; Ling, M. M.; Cho, K.; Ryu, C. Y.; Bao, Z. N. J. *Am. Chem. Soc.* **2005**, *127*, 11542. (c) Veres, J.; Ogier, S.; Lloyd, G.; de Leeuw, D. *Chem. Mater.* **2004**, *16*, 4543. (d) Chua, L.-L.; Zaumseil, J.; Chang, J.-F.; Ou, E. C. W.; Ho, P. K. H.; Sirringhaus, H.; Friend, R. H. *Nature* **2005**, *434*, 194.

(12) (a) Tang, M. L.; Okamoto, T.; Bao, Z. N. *J. Am. Chem. Soc.* **2006**, *128*, 16002. (b) Ong, B. S.; Wu, Y. L.; Liu, P.; Gardner, S. *J. Am. Chem. Soc.* **2004**, *126*, 3378. (c) Kobayashi, S.; Nishikawa, T.; Takenobu, T.; Mori, S.; Shimoda, T.; Mitani, T.; Shimotani, H.; Yoshimoto, N.; Ogawa, S.; Iwasa, Y. *Nat. Mater.* **2004**, *3*, 317. (d) *Organic Field Effect Transistors*; Bao, Z., Locklin, J., Eds.; CRC Press, Taylor & Francis Group: Boca Raton, FL, 2007; (e) Gundlach, D. J.; Kuo, C. C.; Nelson, S. F.; Jackson, T. N. *57th Annual Device Research Conference Digest*, 1999, *164*.

(13) (a) Lee, H. S.; Kim, D. H.; Cho, J. H.; Hwang, M.; Jang, Y.; Cho, K. *J. Am. Chem. Soc.* **2008**, *130*, 10556. (b) Virkar, A.; Mannsfeld, S.; Oh, J. H.; Toney, M. F.; Tan, Y. H.; Liu, G.-Y.; Scott, C.; Miller, R.; Bao, Z. *Adv. Funct. Mater.* **2009**, *19*, 1962.

(14) Ito, Y.; Virkar, A.; Mannsfeld, S.; Oh, J. H.; Toney, M.; Locklin, J.; Bao, Z. *J. Am. Chem. Soc.* **2009**, *131*, 9396.

(15) (a) Gragson, D. E.; McCarty, B. M.; Richmond, G. L. *J. Am. Chem. Soc.* **1997**, *119*, 6144. (b) Shen, Y. R. *Surf. Sci.* **1994**, *299*, 551. (c) Zhuang, X.; Miranda, P. B.; Kim, D.; Shen, Y. R. *Phys. Rev. B* **1999**, *59*, 12632.

(16) (a) Liu, Y.; Wolf, L. K.; Messmer, M. C. *Langmuir* **2001**, *17*, 4329. (b) Messmer, M. C.; Conboy, J. C.; Richmond, G. L. *J. Am. Chem. Soc.* **1995**, *117*, 8039. (c) Guyotsionnest, P.; Hunt, J. H.; Shen, Y. R. *Phys. Rev. Lett.* **1987**, *59*, 1597. (d) Ji, N.; Ostroverkhov, V.; Chen, C.-Y.; Shen, Y.-R. *J. Am. Chem. Soc.* **2007**, *129*, 10056.

(17) (a) Ye, H.; Huang, J.; Park, J. R.; Katz, H. E.; Gracias, D. H. *J. Phys. Chem. C* **2007**, *111*, 13250. (b) Ye, H.; Abu-Akeel, A.; Huang, J.; Katz, H. E.; Gracias, D. H. *J. Am. Chem. Soc.* **2006**, *128*, 6528.

(18) Youn, J.; Chen, M.-C.; Liang, Y.-j.; Huang, H.; Ortiz, R. P.; Kim, C.; Stern, C.; Hu, T.-S.; Chen, L.-H.; Yan, J.-Y.; Facchetti, A.; Marks, T. J. *Chem. Mater.* **2010**, *22*, 5031.

(19) *Semiconductor Devices: Physics and Technology*; Sze, S. M., Ed.; Wiley: New York, 1985.

(20) Fukuto, M.; Heilmann, R. K.; Pershan, P.; Yu, S. M.; Soto, C. M. *J. Chem. Phys.* **2003**, *119*, 6253.

(21) Ocko, B. M.; Wu, X. Z.; Sirota, E. B.; Sinha, S. K.; Gang, O.; Deutsch, M. *Phys. Rev. E* **1997**, *55*, 3164.

(22) Ong, T. H.; Davies, P. B.; Bain, C. D. *Langmuir* **1993**, *9*, 1836.

(23) Anglin, T. C.; Speros, J. C.; Massari, A. M. *J. Phys. Chem. C* **2011**, *115*, 16027.

(24) Durbin, M. K.; Richter, A. G.; Yu, C. J.; Kmetko, J.; Bai, J. M.; Dutta, P. *Phys. Rev. E* **1998**, *58*, 7686.

(25) Warren, B. E. *X-Ray Diffraction*; Addison-Wesley Publishing Co.: Reading, MA, 1969.

(26) For the present analysis we assumed that for a given P-BTDT crystal, the number of unit cells in the substrate plane is substantially higher than those in the out-of-plane direction. This assumption is not

strictly valid for P-BTDT deposited on AA-OTS. This is because the AFM-derived (SI Figure S9) thickness of crystals of ~13 unit cells (40 nm) is non-negligible in comparison to the GIXRD-derived domain size of ~50 unit cells (33 nm). However, because the amount of P-BTDT deposited on both SAMs is identical, thicker crystals imply a lower surface coverage. This suggests that the derived value of SHH/SAA = 2.6 represents the lower bound for the ratio of surface coverage by crystalline domains.

(27) Matsubara, R.; Ohashi, N.; Sakai, M.; Kudo, K.; Nakamura, M. *Appl. Phys. Lett.* **2008**, *92*, 242108.

(28) McCulloch, I.; Heeney, M.; Bailey, C.; Genevicius, K.; MacDonald, I.; Shkunov, M.; Sparrowe, D.; Tierney, S.; Wagner, R.; Zhang, W.; Chabinyc, M. L.; Kline, R. J.; McGehee, M. D.; Toney, M. F. *Nat. Mater.* **2006**, *5*, 328.

(29) Dodabalapur, A.; Torsi, L.; Katz, H. E. *Science* **1995**, *268*, 270.